Analyzing the FMN – heme interdomain docking interactions in neuronal and inducible NOS isoforms by pulsed EPR experiments and conformational distribution modeling

Andrei V. Astashkin[†], Yadav Prasad Gyawali [‖], Ting Jiang [‖], Haikun Zhang [‖], Changjian Feng[‖,*]

[†] Department of Chemistry and Biochemistry, University of Arizona, Tucson, AZ 85721, USA

[‖] College of Pharmacy, University of New Mexico, Albuquerque, NM 87131, USA

Abstract

Nitric oxide synthases (NOSs), flavo-hemoproteins with relatively rigid domains linked by flexible regions, require optimal FMN domain docking to the heme domain for efficient interdomain electron transfer (IET). To probe the FMN-heme interdomain docking, the magnetic dipole interactions between the FMN semiquinone radical (FMNH$^\bullet$) and the low-spin ferric heme centers in oxygenase/FMN (oxyFMN) constructs of neuronal and inducible NOS (nNOS and iNOS, respectively) were measured using the relaxation-induced dipolar modulation enhancement (RIDME) technique. The RIDME data were analyzed using the mesoscale Monte Carlo calculations of conformational distributions of NOS, which were improved to account for the native degrees of freedom of the amino acid residues constituting the flexible interdomain tethers. This analysis enabled us to estimate the stabilization energies and populations of the docking complexes of calmodulin (CaM) and the FMN domain with the heme domain. The FMN – heme domain docking energies obtained for nNOS and iNOS were similar (-3.8 kcal/mol), in agreement with the high degree of conservation of the FMN – heme domain docking interface. In spite of the similar energetics, the FMN – heme domain docking probabilities in nNOS and iNOS oxyFMN were noticeably different (~ 0.19 and 0.23, respectively), likely due to differences in the lengths of the FMN – heme interdomain tethers and the docking interface topographies. The analysis based on the IET theory and RIDME experiments indicates that the variations in conformational dynamics are likely responsible for half of the difference between the FMN – heme IET rates in the two NOS isoforms.

Introduction

Nitric oxide synthases (NOSs) are multidomain flavo-hemoproteins responsible for the biosynthesis of nitric oxide (NO) in mammals. NO is involved in various biological functions (e.g., vasodilation, immune response), and its production by NOS is tightly controlled by both intrinsic and extrinsic factors, including protein-protein interactions and phosphorylation [1]. Deviant NO production *in vivo* contributes to numerous pathologies (e.g., cancer and stroke). Therefore, deciphering the detailed molecular mechanism of NOS is important for both basic science and therapeutic developments [2-4].

Three mammalian NOS isoforms exist: neuronal NOS (nNOS), inducible NOS (iNOS), and endothelial NOS (eNOS), operating in various systems of the organism. Mammalian NOS is a homodimeric protein. Each subunit is composed of a catalytic heme-containing oxygenase domain (also referred to as heme domain in the NOS field) connected by a calmodulin (CaM) binding linker to a reductase domain. The reductase domain consists of an FAD/NADPH binding subdomain, also referred to as the ferredoxin-NADPH reductase (FNR) subdomain, and an FMN subdomain; these two subdomains are connected by a random coil tether. Note that the prefix "sub" is commonly omitted, and we will follow this practice below. The overall structural layout of NOS confirmed by recent single-particle electron microscopy (EM) studies [5-7] is schematically shown in Figure 1. Note that CaM plays an essential role in NOS function (see below), and the bound CaM is therefore also shown in Figure 1. The NOS domains and bound CaM represent relatively rigid modules, while the random coil tethers joining the NOS domains are flexible, which allows NOS to assume various conformations. It is important to note that AlphaFold 2 has been recently employed not only to predict converged, top structural models of the NOS proteins [8, 9], but also to generate alternative conformations and conformational ensembles [8]. Researchers have started to embrace such AI-based structural modeling methodologies, which can be validated with experimental data and/or used to generate new testable hypotheses. Looking forward, such advancements pave the way for detailed understanding of functional protein dynamics in complex biological systems such as NOSs.

The synthesis of NO from the L-arginine substrate is catalyzed by the heme centers in the oxygenase domain. The electrons required for this process are delivered to the heme centers across the enzyme from the FNR domain. The FAD cofactor receives two electrons from NADPH and donates them, one at a time, to the heme center via the FMN cofactor. The FMN domain acts as a tethered shuttle to transport an electron between the FNR and heme domains. At the endpoints of the FMN domain shuttling motion, the interdomain FAD/FMN and FMN/heme docking complexes are formed, enabling, respectively, the FAD-FMN and FMN-heme interdomain electron transfer (IET) processes [10, 11]. Note that the FMN-heme IET enables the dioxygen binding to the ferrous heme center and subsequent oxidative reactions at the heme active site leading to NO production.

The efficient electron transport across the NOS enzyme is only possible when CaM is bound to the CaM binding region of the flexible tether connecting the FMN and heme domains (Figure 1). The CaM binding to NOS releases the FMN domain from its docking position at the FNR domain and enables the FMN domain shuttling motion. Additionally, CaM docks onto the heme domain alongside the FMN domain [12, 13]. This limits the conformational space available for the FMN domain and further facilitates the productive FMN – heme interdomain docking and efficient IET. CaM binds to iNOS protein at basal [Ca^{2+}], while its binding to nNOS or eNOS only occurs at elevated intracellular Ca^{2+} concentrations [1]. It is of current interest to develop and implement new solution-based techniques (e.g., site-specific infrared spectroscopy [14], crosslinking mass spectrometry [8, 9]) to probe the impact of CaM-binding and map the interdomain interactions. Exploring how CaM binding and the interdomain docking influence the NOS dynamics is crucial for enhancing our foundational comprehension of the NOS isoform regulatory mechanism.

Although the FMN domain shuttling motion is crucial in regulating the efficiency of the electron transport across the NOS enzyme, knowledge of the dynamics and statistics of the corresponding conformational rearrangements is still scanty. The docking probabilities and dynamics for the various modules in the NOS proteins have been extensively studied with various solution-based biophysical methods such as pulsed EPR spectroscopy and single molecule FRET [12, 15, 16], but in most cases, a direct comparison of these experimental data is not straightforward. Besides, we currently lack a unifying computational approach for interpreting the experimental results at a quantitative level and explaining the perceived differences among the experimental results obtained with different methods.

To investigate the conformational properties of NOS, we have recently adopted an approach [17] that synergistically combines the experimental measurements by the relaxation-induced dipolar modulation enhancement (RIDME) technique [18, 19] with Monte Carlo calculations of NOS conformational distributions. The RIDME measurements in that work [17] were performed for spin-labeled CaM; a bifunctional SL (BSL) nitroxide, 3,4-bis-(methanethiosulfonylmethyl)−2,2,5,5-tetramethyl-2,5-dihydro-1H-pyrrol-1-yl oxy, was attached to a T34C/S38C double-mutant CaM, and the spin-labeled CaM was referred to as BSL CaM. The positional distribution of the BSL relative to the heme centers resulting from the calculated conformational distributions of NOS was then used to compute the theoretical RIDME effect and compare it with the experimental one [17]. Using such an approach, we obtained an initial understanding of the conformational distributions of NOS and estimated the stabilization energies for the CaM – heme domain, FMN – heme domain, and FMN – FNR domain docking complexes [17].

The present work advances the investigation of NOS conformational properties by improving our computational methodology and extending the experimental studies to include a new reference module and an additional NOS isoform. Specifically, the computational methodology has been conceptually improved by adopting a more rigorous approach to describing the conformational mobility of the protein random coil using the proper rotations around the N-C_a and C_a-C bonds in the protein backbone. The heuristic approach of our previous work [17] was based on random residue-to-residue bend angles within the range derived from surveying several protein structures.

Including a new reference module, the FMN domain, has enabled validation of the previous docking energy estimates [17]. The former analysis was based on the RIDME experimental data obtained for BSL CaM supplemented by certain assumptions regarding the docking probability of the FMN domain. These assumptions have created an uncertainty in the estimated CaM – heme domain and FMN – heme domain docking energies (E_d(CaM) and E_d(FMN), respectively). To address this ambiguity, we report herein on a RIDME measurement and analysis for the FMN semiquinone radical ($FMNH^\bullet$) in the nNOS oxyFMN construct. The oxyFMN construct contains only the oxygenase and FMN domains connected by the CaM-binding tether. Compared to the full-length protein shown in Figure 1, it lacks the FNR domain and the tether joining the FMN and FNR domains. The $FMNH^\bullet$ RIDME data obtained in this work complement the RIDME data obtained for BSL CaM [17] to provide the full experimental data set necessary for an unbiased analysis of the nNOS conformational distribution.

Finally, we have extended the investigation to include iNOS oxyFMN under similar conditions. In the iNOS case, the study of the BSL CaM – heme interaction is impossible because CaM is tightly bound to cysteine-rich iNOS, which precludes the site-specific spin labeling for the CaM-iNOS complex. However, the FMNH$^\bullet$ – heme interaction in iNOS is accessible and can be used for estimating the FMN – heme domain docking energy and probability (subject to assumptions about E_d(CaM)). These parameters can then be related to the observed difference between the FMN – heme IET rates in iNOS and nNOS.

Materials and Methods

EPR sample preparation. Expression and purification of rat nNOS oxyFMN and human iNOS oxyFMN proteins were conducted using our previously reported protocols [12, 20]. The iNOS protein must be co-expressed with CaM. The purified NOS protein was partially reduced to the FMNH$^\bullet$/low spin Fe(III) form [20]; the sample preparation and transfer setup are depicted in Figure 2A. Briefly, the protein was first buffer-exchanged into a deuterated solution (100 mM Bis-Tris propane, 200 mM NaCl, 2.5 mM $CaCl_2$, 3 mM imidazole, 43% d_6-ethylene glycol, pD 7.2) using a spin concentrator at low temperature. The protein solution was pipetted and intermittently mixed to mitigate potential aggregation caused by higher concentrations of ethylene glycol near the membrane. 400 μL of the deuterated solution in a capped cuvette (Starna Cells, Inc., CA, USA) was vigorously bubbled by D_2O-saturated argon gas for 30 minutes, and the NOS protein sample was injected and purged by argon gas over the protein sample surface for another 30 minutes in an ice bucket; this is to displace oxygen via diffusion across the solution surface. Final concentrations were 99 and 97 μM for iNOS and nNOS oxyFMN proteins, respectively; 350 μM CaM was also added into the nNOS sample. The protein sample in the capped cuvette was then titrated with aliquots of freshly prepared dithionite under anaerobic conditions to maximize the yield of $FMNH^\bullet$ (while ensuring a sufficient level of low spin Fe^{3+}), which was monitored by UV-vis spectroscopy (Figure 2B). The sample was then transferred into an EPR tube under positive argon pressure (Figure 2A); the yield of $FMNH^\bullet$ was significantly decreased if the sample transfer was performed without argon purging. The UV-vis spectrum of the partially reduced protein sample inside the EPR tube was measured to confirm that the $FMNH^\bullet$ intermediate was not lost during the sample transfer. The sample was flash-frozen in liquid nitrogen.

Of note are two differences between the current EPR samples and the sample used in our previous iNOS oxyFMN study [20]: (i) the total NOS concentration (~ 100 μM) of the current samples is much lower because our goal here is to investigate the long-range dipole interactions sensitive to the distant aspects of the conformational distribution; (ii) deuterated buffer was used to reduce the effect of spectral diffusion on the electron spin echo (ESE) signal decay and extend the range of measurable distances. More detailed considerations related to the sample deuteration, and the choice of concentration are described in Supporting Information.

Pulsed EPR measurements. The pulsed EPR experiments were performed on a home-built K_a-band pulsed EPR spectrometer [21] at the microwave (mw) frequency of 34.524 GHz. The magnetic field in the measurements, $B_o = 1231.5$ mT, corresponded to the maximum of the ESE field sweep spectrum of $FMNH^\bullet$. The spectrometer was equipped with a helium flow system based on a CF935 cryostat (Oxford Instruments).

The RIDME experiments were performed using two different pulse sequences (see Figure S1). The four-pulse sequence [22] representing a minimal refocused stimulated ESE pulse sequence was used for the measurements in a broad range (40 ns – 1.5 μs) of preparation time interval t_p. To cover the range of $t_p < 40$ ns, the dead-time-free five-pulse sequence [23] was used. Note that the interval t_p is pulse sequence-specific and is defined in Figure S1.

The five-pulse RIDME traces obtained in our measurements extended to $t_p = 285$ ns, so their t_p ranges overlapped with those of the four-pulse RIDME traces. This overlapping region allowed us to scale the four-pulse traces to the correct relative amplitude. The five-pulse and the scaled four-pulsed RIDME traces obtained for each NOS isoform were then combined into a single trace, in which the part at $t_p < 40$ ns was taken from the five-pulse trace, the part at $t_p \in [40$ ns, 285 ns$]$ represented an average between the corresponding parts of the five- and four-pulse traces, and the part at $t_p > 285$ ns was taken from the four-pulse trace. In the discussion of experimental results below, this resulting combined RIDME trace is referred to simply as a RIDME trace.

The relaxation interval, T_R, was equal to 65 μs in both pulse sequences. The lengths of the 90° and 180° pulses were 14 ns and 22 ns, respectively. More complete timing details are described in the Figure S1 caption in the Supporting Information. The measurements were performed at two temperatures, $T_{low} = 7$ K and $T_{high} = 20$ K, chosen to satisfy certain criteria for the longitudinal relaxation rates of the low-spin heme centers, as discussed in the Results and Discussion section. The overall measurement protocol and relevant details are discussed in the literature [17, 19] and, briefly, in Results and Discussion section.

Pulsed EPR numerical simulations. The pertinent details of the numerical simulations of the RIDME traces were described previously [17]. In particular, as a necessary approximation, the g-factor of the heme centers in the simulations is considered to be isotropic and equal to $g_{iso} = 2.22$ (corresponds to the imidazole-coordinated low-spin heme center of NOS). The g-anisotropy of the heme centers was neglected because the orientations of their g-frames are not known. The unpaired electron spin on FMNH$^{\bullet}$ was considered to be located on its N5 atom.

NOS protein conformation modeling. The Monte Carlo computational approach to predicting NOS conformational statistics was described previously [17]. The computations were performed on a mesoscopic scale, where the amino acid residues of the flexible interdomain tethers, the NOS domains (except the heme domain), and the bound CaM were modeled by hard spheres of appropriate diameters (e.g., Figure S2). In this work, we improved this approach by considering the native mobility in the amino acid chain instead of a heuristic approach based on the uniformly distributed spherical angles. The details are described in the Results and Discussion section.

Results and Discussion

General approach to structural analysis. The common approach in protein structural analysis based on pulsed EPR measurements, including double electron-electron resonance (DEER) and RIDME, is to estimate the distance and/or distance distribution for the studied pair of paramagnetic centers and then use this information to reveal certain structural aspects of the protein system. Obtaining a reasonably accurate distance distribution directly from the time domain experimental data generally requires collecting these data with a high signal/noise ratio and in a wide range of preparation time intervals that ideally should be broad enough as to allow the spin pair-related DEER or RIDME effect to (nearly) reach its asymptotic values. Notably, the regular robust methods for determining the distance distribution [24] are developed for a pair of interacting paramagnetic centers and cannot be used without modifications for more complicated systems consisting of three or more spins.

The large structural flexibility of the NOS protein results in a wide (tens of Å) distribution of the distances between the tethered module partners (e.g., heme and FMN domains, heme domain and bound CaM). The actual experimental RIDME data obtained in this work (see below) would not allow one to directly estimate these distance distributions with any accuracy. An additional factor that would complicate such analysis is that we are dealing with a three-spin system because the observer spin (e.g., BSL attached to CaM or FMNH$^{\bullet}$ in the FMN domain) simultaneously interacts with two heme centers in the dimeric heme domain. The only meaningful solution to the problem in such a situation is the approach we developed in our previous work [17]. Specifically, we employ the Monte Carlo calculation of NOS conformational distribution based on the structural properties of the system (sizes of rigid modules, degrees of freedom allowed by the connecting tethers) and compare the RIDME trace calculated for this distribution with the experimental one.

With such an approach, the docking energies represent the model parameters that provide the flexibility in adjusting the calculated structural distributions. The overall goal of the analysis is to estimate these energies and some of the resulting structural properties of the system (e.g., the populations of the docked states). The sufficiency requirements to the experimental data (e.g., how long the recorded RIDME trace should be) in this approach are greatly diminished as only certain types of distance distributions are possible, and correspondingly, the range of allowed variation in the RIDME data is severely limited. This situation is somewhat similar to the problem of estimating a mathematical function based on a limited number of data points. For example, an infinite number of possible functions can fit two data points, but only one straight line can be drawn through them. The complexity and specific details of the structural model may now play a greater role in affecting the potential error in the obtained model parameters (e.g., docking energies) than extending the experimental data beyond the minimally sufficient range.

Calculations of conformational distributions. The calculations of NOS conformational distributions were performed using the mesoscopic approach described in [17]. Briefly, the heme domain is represented by the actual crystal structure (pdb 4JSH for rat nNOS and pdb 1NSI for human iNOS). The bound CaM, FMN domain, and FNR domain are represented by spheres whose diameters approximately correspond to the characteristic sizes of these modules: 36 Å for bound CaM, 32 Å for the FMN domain (Figure S2), and 40 Å for the FNR domain. Note that the FNR domain is only present in the full-length NOS, but not in the oxyFMN construct. The amino acid residues of the random coil tether joining the NOS domains are represented by spheres of 3.8 Å diameter (corresponding to the distance between the consecutive C_α atoms). A random conformation of the flexible chain is generated using the angular degrees of freedom describing the possible relative orientations of adjacent chain elements (tether residues and the larger modules) and applying the steric constraints that do not allow the chain elements to penetrate each other (self-avoiding chain), the heme domain, and the second flexible chain growing out of the other subunit of the homodimeric heme domain.

The docking interactions as a function of distance, R_{ref}, were modeled by an exponential potential with the characteristic decay length, R_{o}, of 5 – 10 Å. Such a model is suitable for describing both the specific electrostatic interactions in ionic solutions and the hydrophobic interactions between the large modules [17]. At short distances, the exponential model for these interactions is expected to become invalid, and therefore, the potential at $R_{\mathrm{ref}} < 5$ Å, was assumed to be constant. The probability of a given conformation in thermal equilibrium was taken proportional to $\exp(-E_{\mathrm{d}}/kT_{\mathrm{ef}})$, in accordance with Boltzmann law, where E_{d} is the total docking energy, k is the Boltzmann constant, and T_{ef} is the effective temperature corresponding to the conformational distribution. For our samples and EPR experimental conditions, T_{ef} is estimated as ~ 200 K (see Supporting Information for details).

The distance R_{ref} for CaM was defined as that between the positions of C_{α} atom of the CaM residue A103 in a given conformation and in the predicted docking complex; A103 is located at the CaM – heme domain docking interface, and it is one of the residues closest to the heme domain surface when the docking complex is formed. For the FMN domain, R_{ref} was defined as the distance between the position of the FMN N5 atom in a given conformation and in the predicted docking complex. If R_{ref} for a given module in a certain conformation was less than 5 Å, this module was considered to be docked. Obviously, this definition of the docked state is simplistic and does not fully reflect the exact shape and volume of the conformational space that corresponds to the docked state in the actual protein. This fact should be considered when comparing the calculated docking probabilities with the values obtained from various experimental measurements.

The specific difference between the previous [17] and current calculations is in how we generate the orientation of the next residue or a larger module out of the given one, which represents a key step in modeling the random coil tethers. In the heuristic approach of the previous work [17], the position of the next residue was generated using the angles θ and φ of the spherical coordinate system, with θ being uniformly distributed between 20° and 95° (estimated from surveying several protein structures), and φ being uniformly distributed between 0 and 2π. Such chain propagation model is shown on the left-hand side of Figure 3 and is referred to below as a "uniformly distributed spherical angles" (UDSA) model.

In this work, we have adopted a more rigorous approach that properly accounts for the structure and actual degrees of freedom of the peptide fragment. These degrees of freedom, as discussed by Ramachandran *et al*. [25] to explain protein folding patterns, represent the rotations by angles φ and ψ around the N-C$_\alpha$ and C$_\alpha$-C bonds (see the right-hand side panel of Figure 3). The range limits available to these angles are determined by the electrostatic repulsion between atoms of the consecutive peptide fragments. In this study, the random coil tethers were modeled by polyalanine chains. The interatomic interactions were approximated by Lennard-Jones potentials [26], and the whole chain propagation model is therefore called "Ramachandran plus Lennard-Jones" (RLJ). The map of electrostatic energies calculated as a function of φ and ψ is shown in Figure S3, and the corresponding map of conformation probabilities in thermal equilibrium at T_{ef} = 200 K is shown in Figure 4. The high-probability areas in this map are in general agreement with those predicted by Ramachandran *et al* [25].

With the RLJ model, the step of adding another residue to the chain (a chain propagation step) requires generating a random set of angles φ and ψ characterized by the 2D probability distribution shown in Figure 4. Figures S4 and S5 compare some of the statistical properties (*e.g.*, end-to-end distribution, radius of gyration) of the amino acid chains obtained using the RLJ model with those obtained with the UDSA model. Figures S6 and S7 show the positional distributions of the FMN domain in nNOS oxyFMN as predicted using the RLJ and UDSA models.

These comparisons demonstrate that for the lengths of the tether in the NOS enzymes (10 – 30 residues), the statistical properties of the UDSA and RLJ models are sufficiently similar. Therefore, the results of our earlier work [17], including the calculated conformational distributions and domain interaction energies, are still valid and do not need to be revised with the introduction of the new calculation model. Indeed, the BSL CaM RIDME traces calculated with UDSA and RLJ models are virtually indistinguishable (see Figure 5).

Thus, the UDSA and RLJ models are equally suitable for calculating the conformational statistics of the random coil tethers that are adequately approximated by the polyalanine chain. However, if the chain contains a considerable proportion of proline residues, this similarity may break because the conformational degrees of freedom then become restricted due to the presence of the pyrrolidine ring. Using the RLJ model that incorporates conformational probability maps accounting for the presence of proline provides an obvious way forward in such a situation. Furthermore, the RLJ model can be readily expanded to include more accurate residue-specific conformational probability maps that will account for bulky side chains in some of the residues (e.g., Trp, Tyr, Phe, His, Arg). We also plan to use the RLJ model in calculating the conformational dynamics of the random coil. The current implementation of the RLJ model represents the first crucial step laying the groundwork for these future developments.

Analysis of RIDME data for FMNH$^\bullet$ in NOS. The collection and analysis of RIDME data for FMNH$^\bullet$ mostly follows our earlier procedure for BSL CaM [17], with the only exception being the method of accounting for the matrix contribution (see below). Briefly, the RIDME trace is obtained as a quotient of the time domain traces recorded using the four-pulse or five-pulse RIDME sequence as a function of the appropriate preparation time interval t_p (see Figure S1) at two temperatures, T_{low} and T_{high}. The choice of these temperatures depends on the longitudinal relaxation of the ferric heme centers in the oxygenase domain. At T_{low}, the T_1 relaxation time of the heme centers is much longer than the relaxation interval of the pulse sequence, T_R (the constant time interval between the second and third mw pulses), while at T_{high}, the heme relaxation during T_R runs to completion.

The T_1 temperature dependences for the low-spin ferric heme centers in iNOS and nNOS were reported in our previous studies [12, 17, 20]. These dependencies are remarkably similar, which is expected given similar coordination environments of the Fe(III) ions in the heme centers and the conserved overall structure of the oxygenase domains of different NOS isoforms. This allows one to use the same temperatures and relaxation intervals in RIDME experiments with nNOS and iNOS. In this work, $T_{\text{low}} = 7$ K, $T_{\text{high}} = 20$ K, and $T_{\text{R}} = 65$ μs were used. These parameters were similar to those in our previous work where $T_{\text{low}} = 8$ K was used. The T_1 values for the low-spin ferric heme centers in both studied NOS isoforms are in the milliseconds at 7 K (or 8 K) and about 15 μs at 20 K. Thus, the heme relaxation during $T_{\text{R}} = 65$ μs can be neglected at 7 K (or 8 K), while it is essentially complete at 20 K.

The quotient FMNH$^\bullet$ RIDME trace is contributed to by the effects of the magnetic dipole interactions between FMNH$^\bullet$ and ferric heme centers within the NOS protein (the intramolecular contribution) and between FMNH$^\bullet$ and ferric heme centers of other NOS proteins uniformly distributed in solution (the intermolecular or matrix contribution). In the present work, the matrix contribution to RIDME was calculated based on the known sample concentration and excluded from the experimental RIDME effect. The details of this calculation are described in Supporting Information, and the matrix decay time in our conditions was estimated as $\tau_{\text{m}} = 12$ μs. In addition, the FMNH$^\bullet$ transverse relaxation time, T_2, is generally temperature-dependent, which may also result in a contribution to the RIDME trace. The change in T_2 was accounted for by taking a quotient of the two-pulse ESE decays recorded at T_{low} and T_{high}.

FMNH$^\bullet$ RIDME in nNOS oxyFMN. We previously found that the RIDME traces for BSL CaM in nNOS can be simulated for a wide range of CaM and FMN domain docking energies, with E_{d}(CaM) and E_{d}(FMN) being negatively correlated [17]. To narrow the range of E_{d}(CaM) and E_{d}(FMN) values, additional information was introduced in the form of docking probabilities for

CaM (P_d(CaM) ~ 0.1-0.2) and FMN domain (P_d(FMN) ~ 0.2-0.4) estimated in earlier pulsed EPR [12] and FMN fluorescence lifetime measurements [27, 28], respectively. The relatively large uncertainty in the estimates partly comes from the fact that the size and shape of the docked state in our computations do not exactly correspond to those of the docked state in the actual experimental systems.

Figure 6 shows examples of FMNH$^\bullet$ RIDME traces calculated for nNOS oxyFMN. Trace 1 is calculated for the quasi-uniform distribution corresponding to E_d(CaM) = E_d(FMN) = 0. In this case, P_d(FMN) ~ 0, the FMN position is distributed in wide limits, and the RIDME trace therefore represents a smooth monotonically decaying curve. The other three traces were calculated for the pairs of E_d(CaM) and E_d(FMN) values that produce a reasonable agreement between the calculated and experimental RIDME results for BSL CaM [17]. These calculated traces in Figure 6 are sufficiently different to demonstrate that the FMNH$^\bullet$ RIDME and BSL CaM RIDME can be used in combination to reach a unique set of E_d(CaM) and E_d(FMN) values without the need for any external/additional information (e.g., the docking probabilities). None of the shown calculated traces in Figure 6 actually fits the experimental FMNH$^\bullet$ RIDME trace. The calculations to achieve such a fit are described below.

In addition to the monotonic decay, the traces calculated for nonzero E_d(FMN) and E_d(CaM) exhibit oscillatory components originating from the FMN – heme domain docking complex, which is characterized by the distances between the FMNH$^\bullet$ and the two heme centers of about 19 Å and 45 Å (as obtained from the docking models [10,27]). These distances result in high- and low-frequency oscillations (~ 8 MHz and ~ 0.6 MHz), respectively.

The experimental RIDME trace obtained for FMNH$^\bullet$ in nNOS oxyFMN is shown in Figure 7a by the black line. To simulate this trace, we used various combinations of E_d(CaM) and

E_d(FMN) values that allowed us to simulate the BSL CaM RIDME trace in our previous work [17] and selected the pairs that provided a reasonable agreement with the experimental data. We started our calculations from $E_d(\mathrm{CaM}) = -4.5kT_{ef}$, $E_d(\mathrm{FMN}) = -10.5kT_{ef}$, and then varied these parameters to reach an agreement between the simulated and experimental traces. Our final estimates are $E_d(\mathrm{CaM}) = (-4.7 \pm 0.2)kT_{ef}$, $E_d(\mathrm{FMN}) = (-9.5 \mp 0.1)kT_{ef}$; "∓" is used for the latter energy because E_d(CaM) and E_d(FMN) that provide a fit to the RIDME effect are anticorrelated. The red trace in Figure 7a shows the simulation result for $E_d(\mathrm{CaM}) = -4.7kT_{ef}$, $E_d(\mathrm{FMN}) = -9.5kT_{ef}$. The resulting CaM and FMN domain docking probabilities are, respectively, about 0.17 and 0.19.

It is clearly evident that the initial high-frequency oscillation in the simulated trace is much more pronounced than in the experimental one, where it is almost unobservable (Figure 7). This is most likely caused by a distribution of the FMN domain docking positions, which results in a distribution of the FMN – heme distances and an efficient averaging-out of the high-frequency oscillation; for example, the change of the FMN – heme distance by 5 Å, from 19 to 24 Å, would result in a two-fold change of the high oscillation frequency, which is proportional to R^{-3}. Over time, we made several attempts to detect the high-frequency oscillations caused by FMNH$^{\bullet}$ – heme dipole interaction in various NOS systems, but only in a few preparations was this detection successful, one of which was iNOS oxyFMN [20]. Unfortunately, we are currently not in the position to address this point in detail because the approximations made in our calculations (e.g., the isotropic g-factor of the heme centers, a specific size and shape of the docking spot, etc.), whereas suitable for the distributed conformations, are not appropriate for accurate calculations of the oscillations coming from the docked state; see the related discussion in our previous works [20, 29]. However, the asymptotic value of the RIDME effect solely depends on the docking probability and does not depend on the structural specifics of the docked state and the frequency and damping of the resulting high-frequency oscillation. Thus, our current inability to properly model the details of the docked state structure has little impact on the analysis of the RIDME trace, whose decay rate is determined by the low-frequency oscillations coming from both the undocked and docked conformations; note that the relative effect of the structural distribution in the docked state on the low-frequency component, which corresponds to the FMN – heme distance of ~ 45 Å, is minor. The same considerations fully apply to the FMNH$^\bullet$ RIDME in iNOS oxyFMN discussed next.

FMNH$^\bullet$ RIDME in iNOS oxyFMN. The experimental FMNH$^\bullet$ RIDME trace obtained for iNOS oxyFMN is shown in Figure 7b by the black line. The calculations of iNOS oxyFMN conformational distributions needed to interpret the experimental RIDME effect were generally similar to those performed for nNOS. The heme domain structure was represented by pdb 1NSI. The tether joining the heme domain and bound CaM was represented by residues 494 – 514, and the tether between bound CaM and FMN domain was represented by residues 528 – 536. The docking positions of CaM and FMN domain at the heme domain were based on the docking model [30].

For iNOS, we cannot perform the BSL CaM RIDME measurements because CaM is tightly bound to cysteine-rich iNOS and cannot be site-specifically spin-labeled. Therefore, to interpret the FMNH$^\bullet$ RIDME data, we performed calculations for various pairs of E_d(FMN) and E_d(CaM) values. The acceptance criteria for a given set of docking energies were (i) an agreement between the calculated and experimental RIDME decays and (ii) sensible magnitudes of the CaM - heme domain docking probability. We have found that the experimental RIDME trace can be approximately simulated for E_d(FMN) $\in$ [$-9.4kT_{ef}$, $-9.9kT_{ef}$], with the corresponding values of

E_d(CaM) ∈ [≤-15kT_{ef}, 0kT_{ef}]. The corresponding ranges of docking probabilities are: P_d(FMN) ∈ [0.19, 0.25] and P_d(CaM) ∈ [> 0.80, 0.004]. At the lower limit of the |E_d(FMN)| values, i.e., E_d(FMN) = -9.4kT_{ef} and E_d(CaM) < -15kT_{ef}, the CaM - heme domain docking probability exceeds 0.8; essentially the system will nearly always be in the docked state, which precludes efficient conformational dynamics. Therefore, this limit is unrealistic. The higher limit of |E_d(FMN)| values is also questionable because P_d(CaM) is approaching zero, which negates the function of CaM in facilitating the FMN – heme docking. We consider, somewhat subjectively, the "reasonable" (in terms of iNOS functionality) range of P_d(CaM) values to be between 0.1 and 0.4. This range reflects our expectation that the docking energies and probabilities in iNOS should be comparable to those in nNOS. With this restraint, the range of the FMN docking energies can be estimated as E_d(FMN) = (-9.6 ± 0.1)kT_{ef}, with the corresponding E_d(CaM) = (-5 ∓ 1)kT_{ef}. These sets of docking energies result in P_d(FMN) = 0.23 ∓ 0.007 and P_d(CaM) = 0.25 ± 0.15. As an example, the red trace in Figure 7b shows a simulation for E_d(FMN) = -9.55kT_{ef} and E_d(CaM) = -5kT_{ef}.

The estimated FMN – heme domain docking probability significantly exceeds the value of 0.16 determined from the fluorescence lifetime measurements [31]. The most likely reasons for this discrepancy are as follows. First, the size and shape of the docked state as used in our calculations are somewhat arbitrary and almost certainly are not exactly the same as those in the actual system (in particular, from the viewpoint of fluorescence lifetime measurements). The second reason is that the effective temperature of the "frozen" conformational distribution in our measurements (T_{ef} ~ 200 K) is lower than the temperature of the fluorescence lifetime measurements (~ 300 K). Lower temperature would favor the docking state due to the Boltzmann factor.

The docking energies and probabilities obtained above are summarized in Table 1. The absolute energy values estimated based on T_{ef} = 200 K are also presented. It is of note that the E_{d}(FMN) values in nNOS and iNOS are very similar. This is not surprising because the FMN – heme domain docking interface is largely conserved between these two NOS isoforms [32, 33]. Given this fact and taking into account that P_{d}(FMN) is mostly determined by E_{d}(FMN) (rather than E_{d}(CaM)), one can conclude that the difference in P_{d}(FMN) values found for these NOS isoforms obviously results from minor differences in topography of the FMN – heme domain docking interface and length of the CaM-bound linkers joining the heme and FMN domains.

One of our motivations in undertaking the comparative FMNH$^{\bullet}$ RIDME analysis for nNOS and iNOS was to evaluate the possible differences between the contributions of the conformational dynamics to the difference between the FMN – heme IET rates in the oxyFMN constructs of these two NOS isoforms (321 s^{-1} in iNOS *vs*. 262 s^{-1} in nNOS [31, 34]). Equation (1) shows the relation between the bulk IET rate and the contributing rate constants [35]:

$$k_{IET} = \frac{k_{ET} k_{on}}{k_{ET} + k_{on} + k_{off}} \tag{1}$$

where k_{IET} is the bulk FMN – heme IET rate measured by laser flash photolysis, k_{ET} is the intrinsic ET rate in the docked state, and k_{on} and k_{off} are, respectively, the rates of formation and dissociation of the FMN – heme domain docking complex. The analysis of conformational contribution to the bulk IET rate in Supporting Information allows one to estimate the possible change in k_{IET} resulting from the changes in large scale conformational dynamics and accessibility of the docked state as $\delta k_{\mathrm{IET}}/k_{\mathrm{IET}}|_{\mathrm{conf}} \in$ [-0.22 - -0.09]; the base value corresponds to iNOS and the δ-incremented one corresponds to nNOS. This accounts for at least half of the overall change in k_{IET} between iNOS oxyFMN and nNOS oxyFMN ($\delta k_{\mathrm{IET}}/k_{\mathrm{IET}} \approx -0.18$). The remaining [-0.09 – 0.04] of the $\delta k_{\mathrm{IET}}/k_{\mathrm{IET}}$ change can be attributed to the variation in k_{ET} of the two NOS isoforms.

It has been discussed in detail [31] that k_{ET} is determined by the interplay of three processes taking place in the docked state: (i) the alignment of the docking complex to the optimal position in terms of the FMN – heme electron tunneling, (ii) the electron tunneling, and (iii) the misalignment from the tunneling position; see Supporting Information for a brief summary of the IET-related processes in NOS. Based on the edge-to-edge FMN-heme distances of ~13 Å in iNOS and ~11 Å in nNOS derived from the docking models [12, 30], the tunneling rate constants, k_t, were estimated as ~10^4 s^{-1} and ~10^5 s^{-1}, respectively [31]. The order-of-magnitude estimates for the domain alignment and misalignment constants in iNOS, based on the analysis of the fluorescence lifetime data [31], are $10^5 – 10^6$ s^{-1}.

The electron tunneling thus appears to be the rate-limiting process among those relevant to the bulk, intrinsic ET rate (Figure S11), and the increased k_t in nNOS should result in a positive δk_{ET}. This outcome, however, can be modified by possible changes in the docking alignment/misalignment rates from iNOS to nNOS, which can counteract the effect of increased k_t. Unfortunately, we are not aware of any experimental information regarding the balance between the various rate constants contributing to k_{ET} in nNOS, and therefore, we will refrain from making any firm conclusions regarding δk_{ET}. However, based on the above considerations, the overall change in k_{ET} is more likely to be either positive or close to zero, and thus we hold the larger absolute values of the conformational contribution to k_{IET} (i.e., $\delta k_{\mathrm{IET}}/k_{\mathrm{IET}}|_{\mathrm{conf}} \sim -0.2$) to be more probable than the smaller ones.

Conclusion

This work represents a necessary step towards a more comprehensive understanding of the roles of major conformational and intrinsic/tunneling components in the FMN – heme IET step in NOS catalysis. We have advanced studies of conformational properties of NOS in three aspects.

First, we have improved the method for calculating the NOS conformational distributions by including the native conformational mobility of the amino acids in the protein random coil fragment. We have then validated our earlier results [17] by showing that the new method (called here RLJ from Ramachandran and Lennard-Jones) produces the RIDME traces for BSL CaM nearly identical to those obtained earlier with a simplified conformational model based on uniformly distributed spherical angles (UDSA). The implementation of the RLJ approach is important from several perspectives: (i) it was not obvious in advance, and had to be verified, that the UDSA and RLJ approaches indeed result in similar estimates of the docking energies and probabilities; (ii) the RLJ approach is more flexible and potentially allows one to account for the differences between the conformational degrees of freedom of various residues (e.g., alanine vs. proline); (iii) the RLJ approach will be used in the mesoscopic calculations of conformational dynamics, where the proper account of the actual degrees of freedom will become a central issue. The work on such calculations is ongoing.

Second, we have acquired and simulated the RIDME traces for $\text{FMNH}^{\bullet}$ in the nNOS oxyFMN construct. The combined use of $\text{FMNH}^{\bullet}$ and BSL CaM RIDME traces (the latter were obtained in [14]) has allowed us to obtain the docking energy estimates for CaM and FMN domain without relying on assumptions about the docking probabilities. The resulting estimates were remarkably close to those reported in our previous work.

Lastly, we have extended the studies to include another NOS isoform, iNOS, and estimated the FMN – heme domain and CaM – heme domain docking energies and populations for this protein. The qualitative analysis based on the NOS IET theoretical model [32] and our RIDME results shows that the variations in conformational dynamics are responsible for at least half of the difference between the FMN – heme IET rates in iNOS and nNOS oxyFMN constructs.

Our combined experimental and computational approach is thus a promising tool for deciphering the conformational properties of NOS, including the CaM – heme domain and FMN-heme interdomain interactions. It can also guide further experiments, e.g., probing molecular mechanism of mutational effects on the IET. The strength and distance dependence of the docking interaction potential(s) derived with our approach represent essential parameters needed for the future mesoscale calculations of NOS conformational dynamics. These tools may open the door for new areas of inquiry into biomolecular dynamics of other tethered modular/multidomain proteins (e.g., sulfite oxidase [36], heat shock protein 70 [37], and numerous other proteins [38]).

Supporting Information.

RIDME pulse sequences used (Figure S1); CaM and FMN domain sizes *vs*. the model spheres (Figure S2); Interatomic interaction energy in Ala-Ala fragment as a function of conformation (Figure S3); Comparison of statistical properties of the RLJ and UDSA models (Figures S4-S7); Original and processed RIDME experimental traces (Figures S8-S10); IET-related processes in NOS and their characteristic rate constants (Figure S11). Considerations regarding the sample deuteration and concentration; Estimating the matrix contribution to RIDME decay; Estimating the effective temperature of the NOS conformational distribution; Estimating the conformational contribution to the bulk IET rate in NOS; Summary of the IET-related processes in NOS.

AUTHOR INFORMATION

Corresponding Author

*Changjian Feng (cfeng@unm.edu)

Author Contributions

The manuscript was written through contributions of all authors. All authors have given approval to the final version of the manuscript.

ACKNOWLEDGEMENT

This material is based upon work funded by NIH GM133973 and NSF 2041692 (CF). This work was also supported in part by National Institutes of Health P20GM130422 and P30ES032755.

ABBREVIATIONS

NO, nitric oxide; NOS, nitric oxide synthase; CaM, calmodulin; nNOS, neuronal NOS; eNOS, endothelial NOS; iNOS, inducible NOS; FNR, ferredoxin-NADPH reductase subdomain; oxyFMN, bi-domain oxygenase/FMN construct of NOS; IET, interdomain electron transfer; BSL, bifunctional spin label; RIDME, relaxation-induced dipolar modulation enhancement; ESE, electron spin echo; DEER, double electron-electron resonance; UDSA, uniformly distributed spherical angles.

Declarations

Conflict of interest The authors declare no conflict of interest.

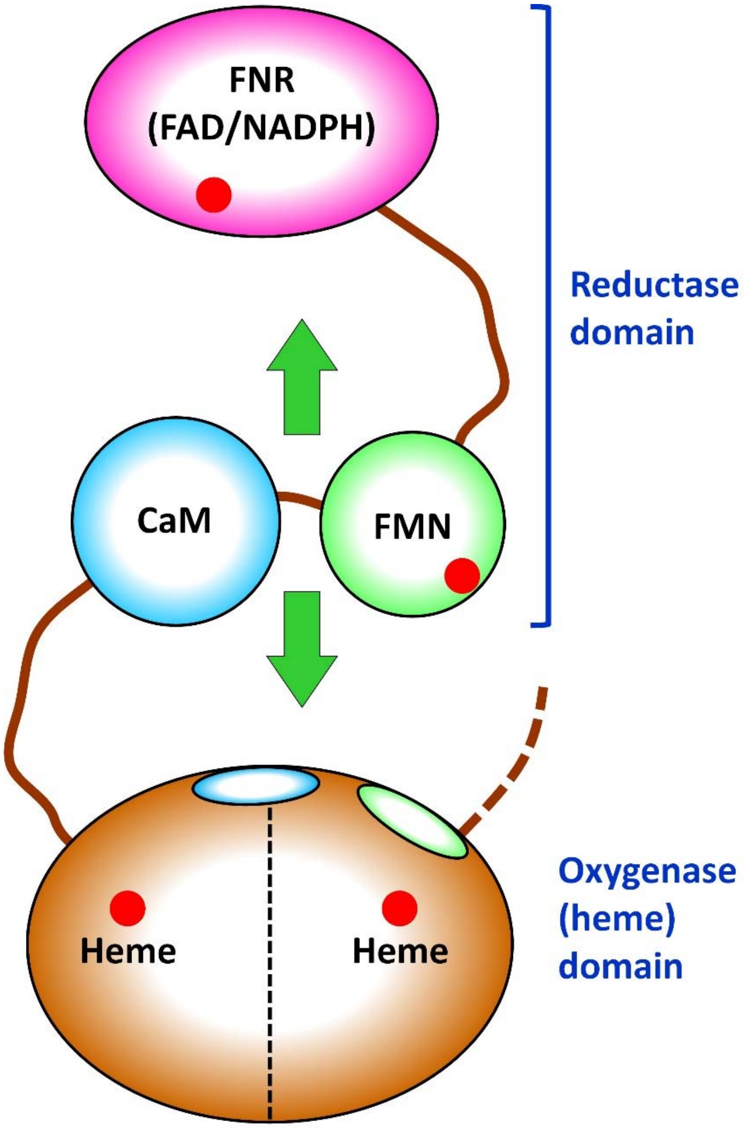

Figure 1. Schematic structural layout of NOS with bound CaM. The red dots in the heme domain indicate the two heme centers, and the vertical dashed line running across the domain indicates its homodimeric nature. The red dots in the FMN and FNR domains indicate the FMN and FAD cofactors, respectively. Only one set of tethered modules (bound CaM and FMN and FNR domains) of the dimeric protein is shown, and the presence of a second set is indicated by the truncated tether growing out of the right-hand side of the heme domain and shown by the dashed line. The light blue- and green-themed spots on the heme domain indicate the docking positions of the shown CaM and FMN domain, respectively; note the inter-subunit FMN-heme docking. The green arrows indicate the structural flexibility of the system.

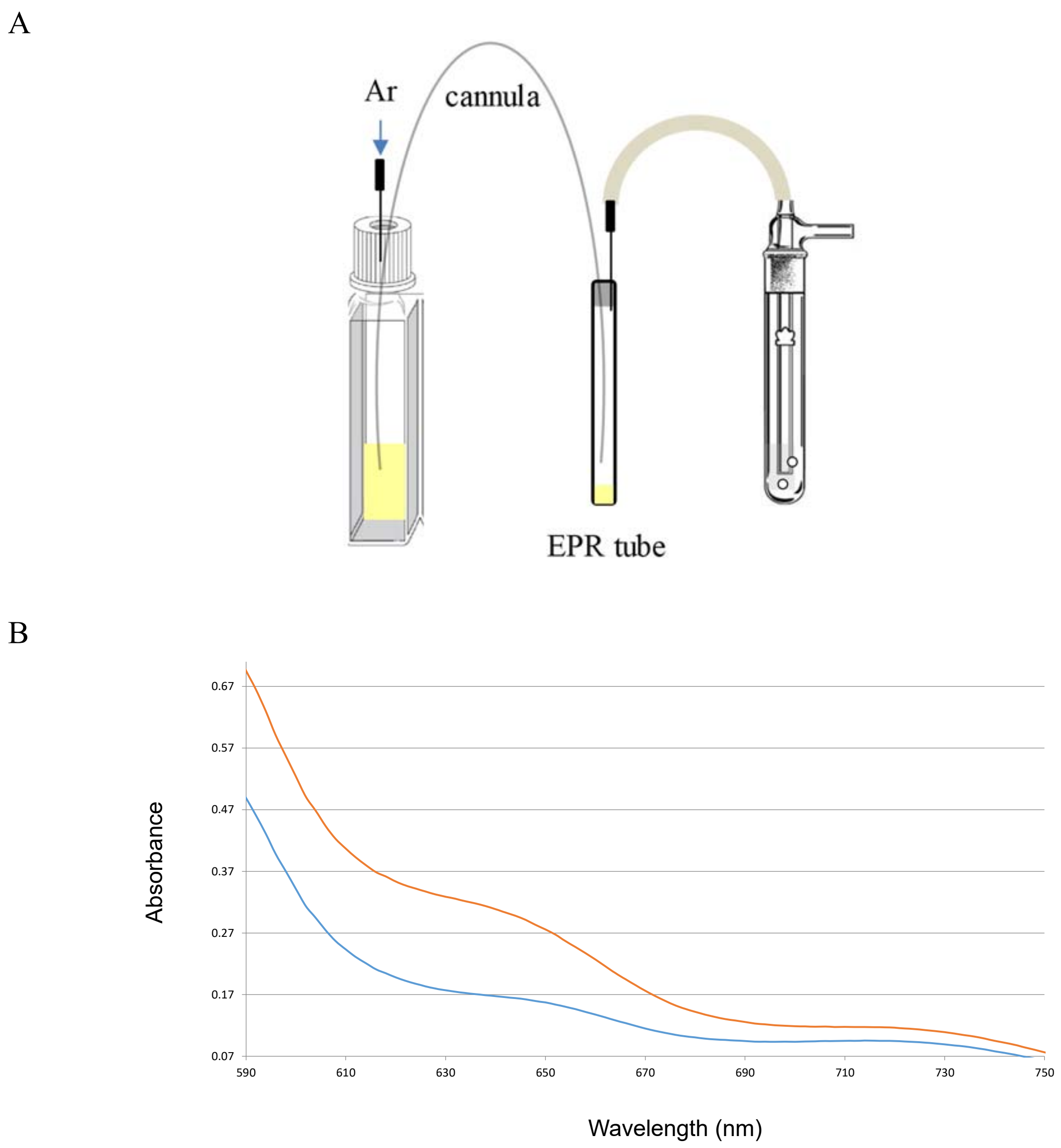

Figure 2. A. Sample transfer into an EPR tube under positive pressure of argon gas. The protein in D_2O buffer solution inside a capped cuvette (Sterna Cells) was first purged with D_2O-saturated argon gas and titrated with fresh prepared dithionite aliquots to maximize the buildup of FMN semiquinone. The reaction was monitored by UV-vis spectroscopy. A cannula was then introduced above the protein solution surface through the septum, with the other end inserted through the septum into the EPR tube (center) and reaching its bottom to flush the inside of the tube with argon. The argon was vented via a syringe needle connected to an oil bubbler (right). After ~ 5 minutes of purging the EPR tube, the cannula in the capped cuvette was immersed into the protein solution to transfer the protein into the tube. The protein sample was frozen in liquid nitrogen, and the EPR tube septum was removed before storing the sample in a liquid nitrogen Dewar. **B.** UV-vis spectra of the human iNOS oxyFMN protein sample before and after adding degassed dithionite aliquots (blue and orange, respectively).

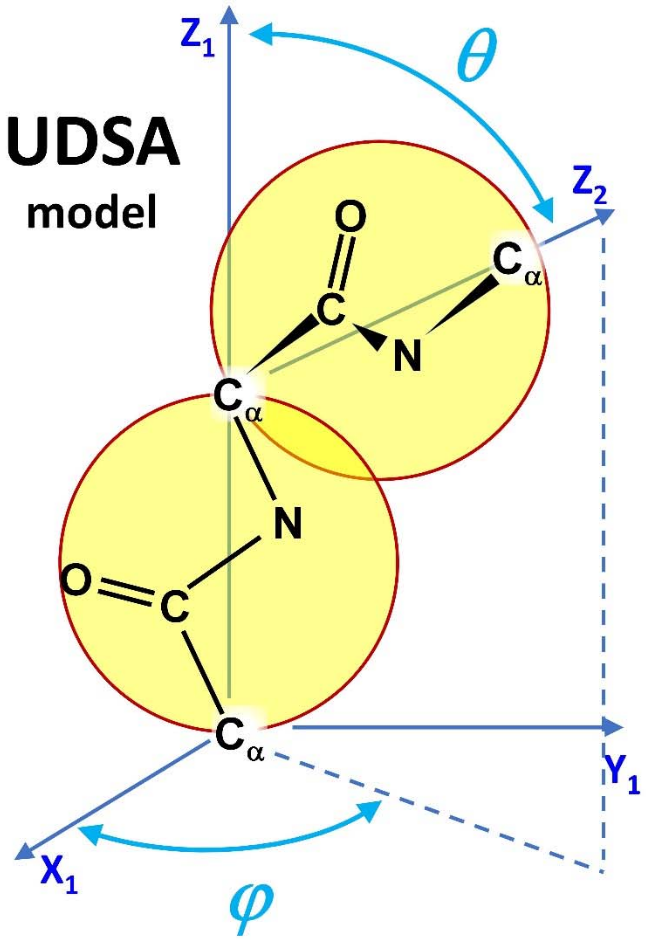
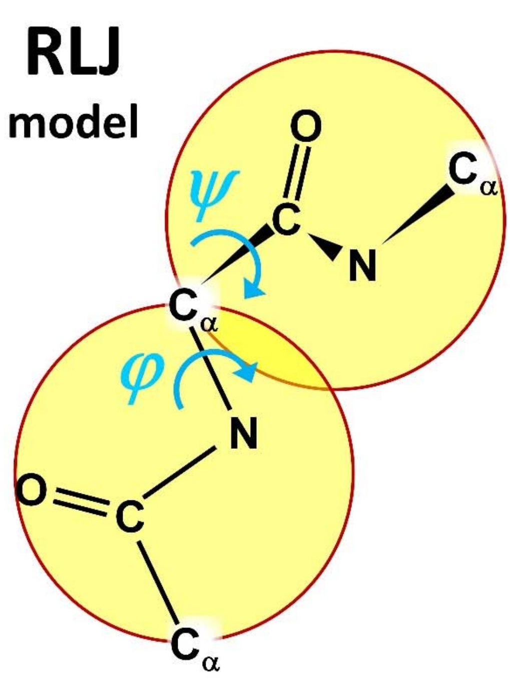

Figure 3. Rotation angles for UDSA and RLJ models.

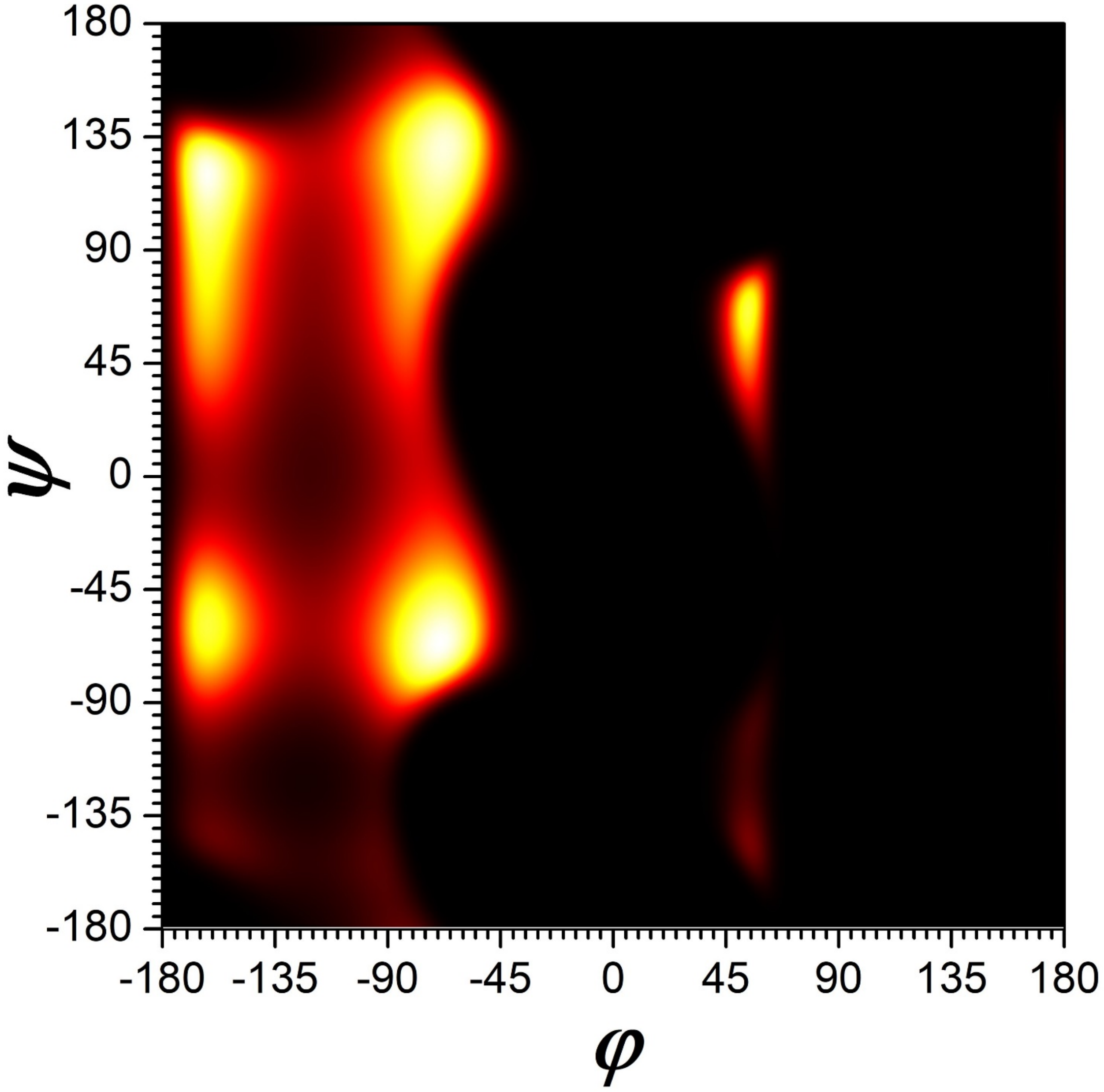

Figure 4. Map of conformation probabilities in thermal equilibrium at T_{ef} = 200 K corresponding to the energy distribution map in Figure S3.

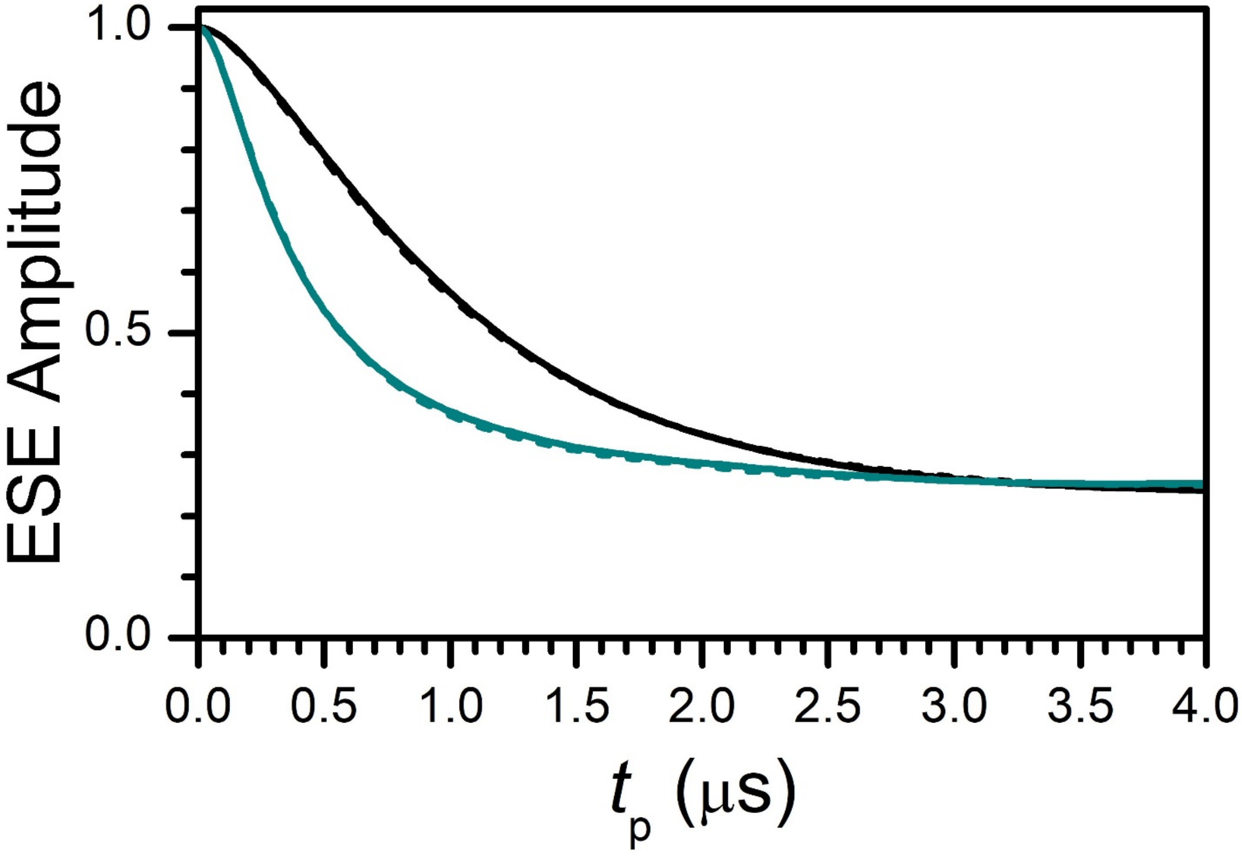

Figure 5. Comparison of RIDME traces calculated for BSL CaM in nNOS using RLJ (solid lines) and UDSA (dashed lines) models. Black traces are calculated for E_d(CaM) = $0kT_{ef}$ and E_d(FMN) = $0kT_{ef}$. Cyan traces are calculated for E_d(CaM) = $-4.5kT_{ef}$, E_d(FMN) = $-10.5kT_{ef}$.

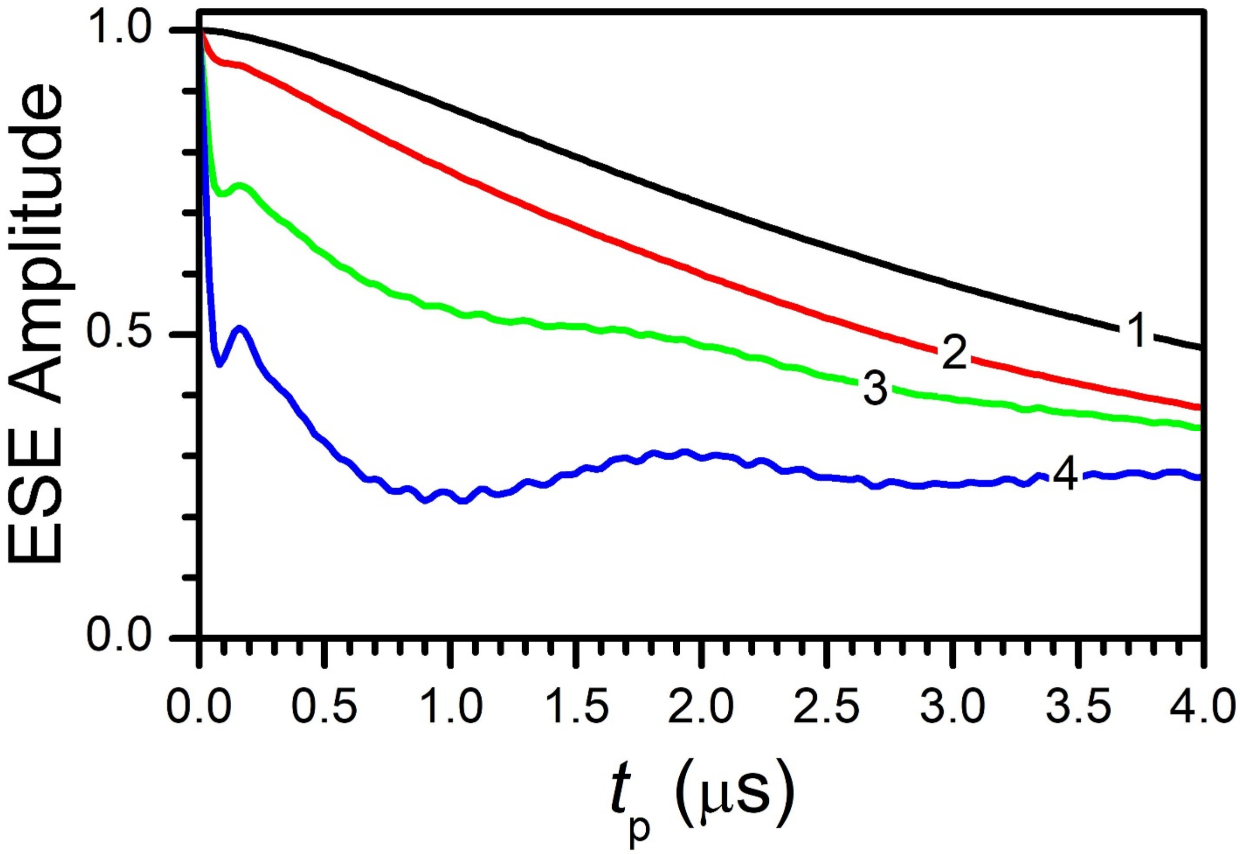

Figure 6. Calculated FMNH$^\bullet$ RIDME traces for nNOS oxyFMN. For traces 1 through 4, (E_d(CaM), E_d(FMN)) = (0, 0)kT_{ef}, (-5.8, -7.5)kT_{ef}, (-4.5, -10.5)kT_{ef}, (-2.2, -14.0)kT_{ef}, respectively.

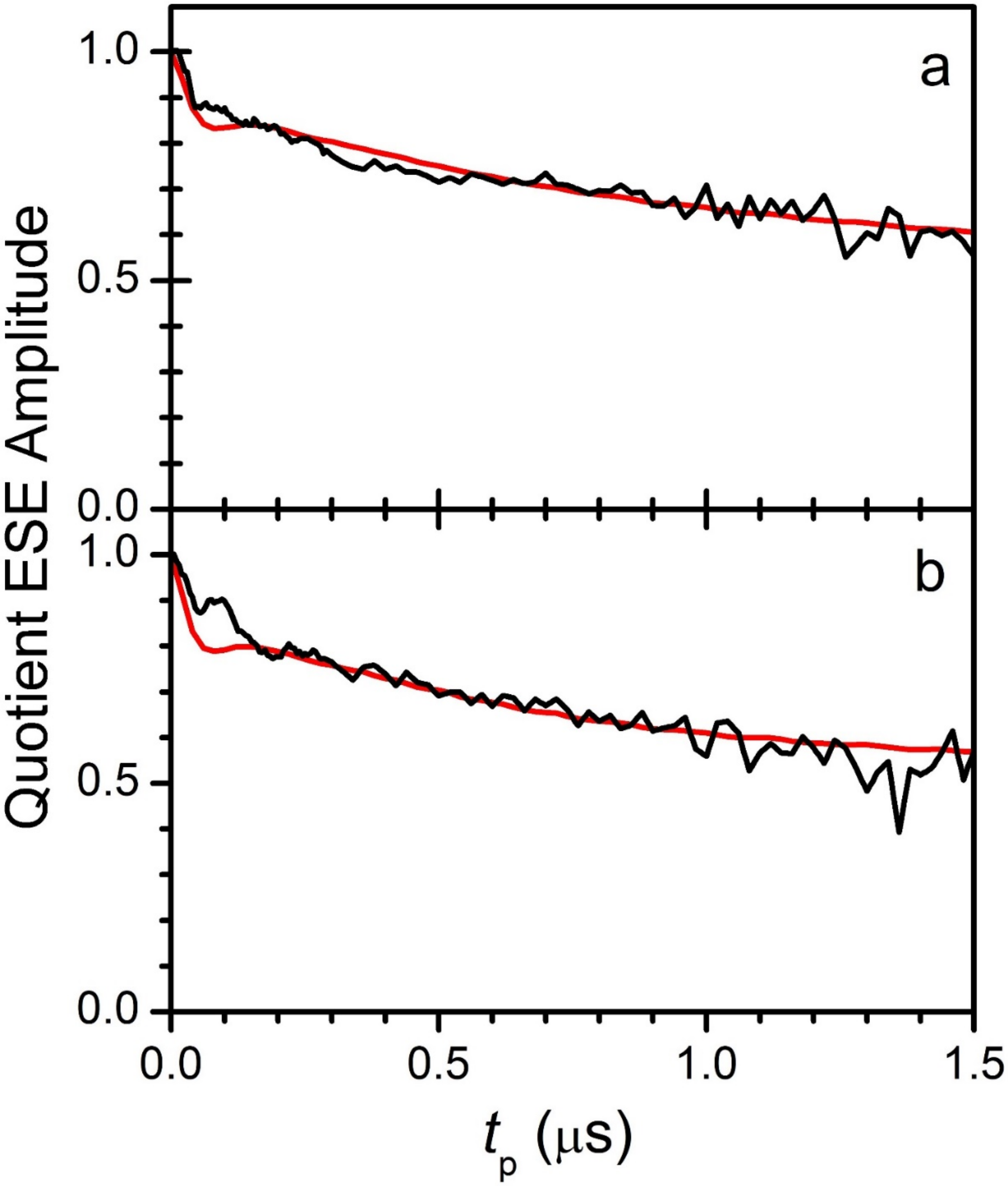

Figure 7. Experimental (black) and simulated (red) RIDME traces for nNOS oxyFMN (panel a) and iNOS oxyFMN (panel b) proteins. The experimental traces were obtained by combining (as described in Materials and Methods) the quotient 5-pulse and 4-pulse RIDME traces shown in Figure S10, which in turn were obtained from the original traces in Figures S8 and S9. The red traces in panels a and b are calculated for (E_d(CaM), E_d(FMN) = (-4.7, -9.5)kT_{ef} and (-5, -9.55)kT_{ef}, respectively.

Table 1. CaM – heme domain and FMN – heme domain docking energies (E_d) and probabilities (P_d) in nNOS oxyFMN and iNOS oxyFMN estimated in this work. The absolute energy estimates (in kcal/mol) are based on T_{ef} = 200 K.

NOS protein	E_d(CaM)	E_d(FMN)	P_d(CaM)	P_d(FMN)
nNOS oxyFMN	$(-4.7 \pm 0.2)kT_{ef}$ $(-1.9 \pm 0.08$ kcal/mol)	$(-9.5 \mp 0.1)kT_{ef}$ $(-3.8 \mp 0.04$ kcal/mol)	0.17 ∓ 0.02	0.19 ± 0.007
iNOS oxyFMN	$(-5 \pm 1)kT_{ef}$ $(-2 \pm 0.4$ kcal/mol)	$(-9.6 \mp 0.1)kT_{ef}$ $(-3.8 \mp 0.04$ kcal/mol)	0.25 ∓ 0.15	0.23 ± 0.007

References

[1] L.J. Roman, P. Martasek, B.S.S. Masters, Chem. Rev. 102 (2002) 1179-1189.

[2] W.K. Alderton, C.E. Cooper, R.G. Knowles, Biochem J 357 (2001) 593-615.

[3] U. Förstermann, W.C. Sessa, Eur. Heart J. 33 (2012) 829-837.

[4] D.J. Stuehr, M.M. Haque, Br. J. Pharmacol. 176 (2019) 177-188.

[5] A.L. Yokom, Y. Morishima, M. Lau, M. Su, A. Glukhova, Y. Osawa, D.R. Southworth, J. Biol. Chem. 289 (2014) 16855-16865.

[6] M.G. Campbell, B.C. Smith, C.S. Potter, B. Carragher, M.A. Marletta, Proc. Natl. Acad. Sci. U. S. A. 111 (2014) E3614-E3623.

[7] N. Volkmann, P. Martásek, L.J. Roman, X.-P. Xu, C. Page, M. Swift, D. Hanein, B.S. Masters, J. Struct. Biol. 188 (2014) 46-54.

[8] T. Jiang, G. Wan, H. Zhang, Y.P. Gyawali, E.S. Underbakke, C. Feng, Biochemistry 63 (2024) 1395-1411.

[9] T. Jiang, G. Wan, H. Zhang, Y.P. Gyawali, E.S. Underbakke, C. Feng, Biochemistry 62 (2023) 2232-2237.

[10] J. Li, H. Zheng, C. Feng, Front Biosci (Landmark Ed) 23 (2018) 1803-1821.

[11] C. Feng, Coord. Chem. Rev. 256 (2012) 393-411.

[12] A.V. Astashkin, L. Chen, X. Zhou, H. Li, T.L. Poulos, K.J. Liu, J.G. Guillemette, C. Feng, J. Phys. Chem. A 118 (2014) 6864-6872.

[13] B.C. Smith, E.S. Underbakke, D.W. Kulp, W.R. Schief, M.A. Marletta, Proc. Natl. Acad. Sci. U. S. A. 110 (2013) E3577-3586.

[14] S. Singh, Y.P. Gyawali, T. Jiang, G.S. Bukowski, H. Zheng, H. Zhang, R. Owopetu, M.C. Thielges, C. Feng, JBIC Journal of Biological Inorganic Chemistry 29 (2024) 243-250.

[15] Y. He, M.M. Haque, D.J. Stuehr, H.P. Lu, Proc. Natl. Acad. Sci. U. S. A. 112 (2015) 11835-11840.

[16] D.C. Arnett, A. Persechini, Q.-K. Tran, D.J. Black, C.K. Johnson, FEBS Lett. 589 (2015) 1173-1178.

[17] A.V. Astashkin, J. Li, H. Zheng, C. Feng, J Phys Chem A 123 (2019) 7075-7086.

[18] L.V. Kulik, S.A. Dzuba, I.A. Grigoryev, Y.D. Tsvetkov, Chem. Phys. Lett. 343 (2001) 315-324.

[19] A.V. Astashkin, in: Z.Q. Peter, W. Kurt (Eds.), Methods Enzymol., vol. Volume 563, Academic Press, 2015, pp. 251-284.

[20] A.V. Astashkin, B.O. Elmore, W. Fan, J.G. Guillemette, C. Feng, Journal of the American Chemical Society 132 (2010) 12059-12067.

[21] A.V. Astashkin, J.H. Enemark, A. Raitsimring, Concepts in Magnetic Resonance Part B-Magnetic Resonance Engineering 29B (2006) 125-136.

[22] L.V. Kulik, Y.A. Grishin, S.A. Dzuba, I.A. Grigoryev, S.V. Klyatskaya, S.F. Vasilevsky, Y.D. Tsvetkov, J. Magn. Reson. 157 (2002) 61-68.

[23] S. Milikisyants, F. Scarpelli, M.G. Finiguerra, M. Ubbink, M. Huber, J. Magn. Reson. 201 (2009) 48-56.

[24] G. Jeschke, G. Panek, A. Godt, A. Bender, H. Paulsen, Appl. Magn. Reson. 26 (2004) 223-244.

[25] G.N. Ramachandran, C. Ramakrishnan, V. Sasisekharan, J. Mol. Biol. 7 (1963) 95-99.

[26] F. Jordan, J. Theor. Biol. 41 (1973) 375-395.

[27] K. Brunner, A. Tortschanoff, B. Hemmens, P.J. Andrew, B. Mayer, A.J. Kungl, Biochemistry 37 (1998) 17545-17553.

[28] D.K. Ghosh, K. Ray, A.J. Rogers, N.J. Nahm, J.C. Salerno, FEBS J. 279 (2012) 1306-1317.

[29] A.V. Astashkin, W. Fan, B.O. Elmore, J.G. Guillemette, C. Feng, J. Phys. Chem. A 115 (2011) 10345-10352.

[30] S.A. Hollingsworth, J.K. Holden, H. Li, T.L. Poulos, Protein Sci. 25 (2016) 374-382.

[31] A.V. Astashkin, J. Li, H. Zheng, Y. Miao, C. Feng, J. Inorg. Biochem. 184 (2018) 146-155.

[32] M.M. Haque, J. Tejero, M. Bayachou, C.T. Kenney, D.J. Stuehr, J. Biol. Chem. 293 (2018) 4545-4554.

[33] J. Tejero, L. Hannibal, A. Mustovich, D.J. Stuehr, J. Biol. Chem. 285 (2010) 27232-27240.

[34] C. Feng, G. Tollin, M.A. Holliday, C. Thomas, J.C. Salerno, J.H. Enemark, D.K. Ghosh, Biochemistry 45 (2006) 6354-6362.

[35] A.V. Astashkin, C. Feng, J. Phys. Chem. A 119 (2015) 11066-11075.

[36] C. Feng, G. Tollin, J.H. Enemark, Biochim. Biophys. Acta 1774 (2007) 527-539.

[37] L. Rohland, R. Kityk, L. Smalinskaite, M.P. Mayer, Proc. Natl. Acad. Sci. U. S. A. 119 (2022) e2123238119.

[38] W.A. Lim, Curr. Opin. Struct. Biol. 12 (2002) 61-68.